Camera Orientation Optimization in Stereo Vision Systems for Low Measurement Error

Xingjian Liu, Wenyuan Chen, Harikrishnan Madhusudanan, Linghao Du, and Yu Sun

***Abstract*—Stereo vision (SV) is widely used for noncontact three-dimensional industrial measurement. In SV systems, camera orientation (the angles formed by the two cameras optical axes across the baseline) is among the factors that influence the measurement accuracy. Presently, there is a great divergence regarding the optimal value of camera orientation, i.e., existing theoretical analyses suggest that the optimal angle lies in 30°–50°; however, a camera orientation angle between 60°–80° is typically used in practical SV systems and commercial products. Unlike previous models that treated system parameters as uncorrelated, the proposed model introduces covariance to model the correlation between camera orientation and the accuracy of detecting corresponding points. The proposed model proves the optimal camera orientation angle lies in 60°–80°, which was verified experimentally via measurements with a circle center tracker (CCT), fringe projection profilometry (FPP), and stereo digital image correlation (DIC).**

***Index Terms*—Accuracy evaluation, error propagation model, stereo vision (SV), 3-D reconstruction.**

I. Introduction

Stereo vision (SV) enables the determination of 3-D coordinates of an object by matching corresponding points from two cameras/images. It is widely used in industrial metrology and diagnosis applications, such as a circle center tracker (CCT) for online positioning [1], fringe projection profilometry (FPP) for 3-D acquisition [2], and stereo digital image correlation (DIC) [3] for deformation and strain measurement. In these applications, accuracy is one of the most crucial specifications for SV systems [4].

The factors governing an SV system's accuracy can be divided into two categories [4], [5]: 1) intrinsic factors including image resolution, signal noise ratio of the image sensor, and lens distortions; and 2) extrinsic factors including system calibration, detection of corresponding points, and camera orientation. The intrinsic factors are largely determined by system hardware. Once the hardware is selected, the extrinsic factors determine the final accuracy of the SV system. Among the extrinsic factors, system calibration involves the determination of intrinsic and extrinsic parameters required for 3-D reconstruction, as illustrated in Fig. 1(a). The detection of corresponding points is an essential step in 3-D reconstruction for finding the same point from two image views, as shown in Fig. 1(b). Methods for both system calibration and corresponding-points detection have been under intense development, and their errors have both been reduced to the subpixel level [6], [7].

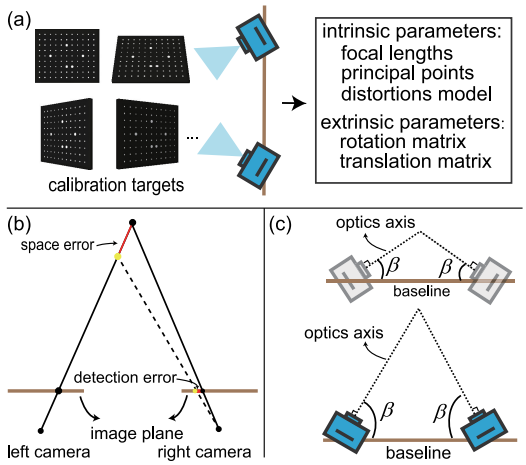

Fig. 1. Three major extrinsic factors that influence the accuracy of an SV system. (a) System calibration [6]. (b) Corresponding points detection [7]. (c) Camera orientation [8].

Camera orientation, referred to the angles formed by the two cameras optical axes across the baseline [see Fig. 1(c) β], determines the error propagation function [5], which indicates how errors in system parameters affect the final reconstructed results. Previous studies revealed that symmetrical camera orientation is necessary for achieving a least measurement error [8]–[12]. However, there is a great divergence regarding the optimal value of camera orientation (angle β). Theoretical analyses suggested that the optimal angle lies in 30°–50° [8]–[10]. In contrast, a camera orientation angle between 60°–80° is typically used in practical SV systems and commercial products [11], [12].

In this article, we propose a new error propagation model for SV systems, which, for the first time, resolves the contradiction of optimal camera orientation between practice and previous theories.

II. Error Propagation Modeling of SV Systems

The first step is to model the geometric setup of an SV system [8]. As shown in Fig. 2, f_L, f_R are focal lengths of the left camera and

Manuscript received May 28, 2020; revised August 3, 2020; accepted August 21, 2020. Date of publication August 25, 2020; date of current version April 15, 2021. The work was supported by the Natural Sciences, and Engineering Research Council of Canada, the Canada Research Chairs program, and the Ontario Research Fund—Research Excellence program. Recommended by Technical Editor H. Wang and Senior Editor H. Qiao. *(Xingjian Liu and Wenyuan Chen contributed equally to this work.) (Corresponding author: Yu Sun.)*

Xingjian Liu, Harikrishnan Madhusudanan, and Linghao Du are with the Department of Mechanical and Industrial Engineering, University of Toronto, Toronto, ON M5S 3G8, Canada, and also with the Robotics Institute, University of Toronto, Toronto, ON M5S 3G8, Canada (e-mail: xj.liu@utoronto.ca; harikrishnan.madhusudanan@mail.utoronto.ca; lh.du@mail.utoronto.ca).

Wenyuan Chen is with the Department of Electrical and Computer Engineering, University of Toronto, Toronto, ON M5S 3G8, Canada, and also with the Robotics Institute, University of Toronto, Toronto, ON M5S 3G8, Canada (e-mail: chenwy.chen@mail.utoronto.ca).

Yu Sun is with the Department of Mechanical and Industrial Engineering, University of Toronto, Toronto, ON M5S 3G8, Canada, and also with the Robotics Institute, the Department of Electrical and Computer Engineering, and the Department of Computer Science, University of Toronto, Toronto, ON M5S 3G8, Canada (e-mail: sun@mie.utoronto.ca).

Color versions of one or more of the figures in this article are available online at https://ieeexplore.ieee.org.

Digital Object Identifier 10.1109/TMECH.2020.3019305

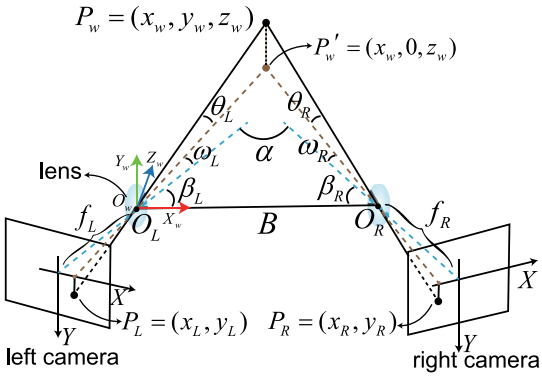

Fig. 2. Geometric setup of an SV system. O_L, O_R and f_L, f_R are optical centers and focal lengths of left and right cameras, respectively, B is the baselines, P_L and P_R represent corresponding points in left and right image planes while P_w is the 3-D point. β_L and β_R are angles formed by the two optical axes across the baseline, i.e., camera orientation.

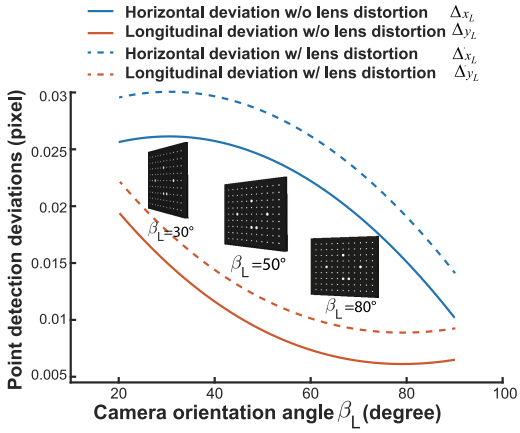

Fig. 3. Relationship between camera orientation (β_L) and detected corresponding point's horizontal and longitudinal deviation (w/ and w/o lens distortions), $(\triangle_{x_L}, \triangle_{y_L})$. A smaller β_L brings more severe perspective distortion and leads to a larger deviation $(\triangle_{x_L}, \triangle_{y_L})$ of point (x_L, y_L).

the right camera, respectively; B is the baseline; $P_L = (x_L, y_L) \in \mathbb{R}^2$ and $P_R = (x_R, y_R) \in \mathbb{R}^2$ represent corresponding points in the left and right image plane; β_L and β_R are angles formed by the two optical axes across the baseline (i.e., camera orientation). The 3-D object point $P_w = (x_w, y_w, z_w) \in \mathbb{R}^3$ is reconstructed by triangulation of the rays from corresponding points P_L and P_R, which is expressed as

$$\begin{cases} x_w = \dfrac{B\cot(\omega_L + \beta_L)}{\cot(\omega_L + \beta_L) + \cot(\omega_R + \beta_R)} \\ y_w = \dfrac{z_w \tan(\theta_L)}{\sin(\omega_L + \beta_L)} \\ z_w = \dfrac{B}{\cot(\omega_L + \beta_L) + \cot(\omega_R + \beta_R)} \end{cases} \tag{1}$$

where ω_L, ω_R and θ_L, θ_R are

$$\begin{cases} \omega_L = \arctan(x_L/f_L),\ \omega_R = \arctan(x_R/f_R) \\ \theta_L = \arctan\left(\dfrac{y_L\cos(\omega_L)}{f_L}\right),\ \theta_R = \arctan\left(\dfrac{y_R\cos(\omega_R)}{f_R}\right) \end{cases}. \tag{2}$$

By combining (1) and the abovementioned equation, $P_w = (x_w, y_w, z_w) \in \mathbb{R}^3$ is expressed as a function of system parameters $\delta = (x_L, y_L, x_R, y_R, \beta_L, \beta_R, B, f_L, f_R)$

$$x_w = \Theta_{x_w}(\delta),\ y_w = \Theta_{y_w}(\delta),\ z_w = \Theta_{z_w}(\delta). \tag{3}$$

According to the error propagation theory [5], the total measurement error e_c of the reconstructed point P_w is obtained by combining the errors of x_w, y_w, z_w, written as

$$e_c = \sqrt{e_{x_w}^2 + e_{y_w}^2 + e_{z_w}^2} \tag{4}$$

where $e_{x_w}, e_{y_w}, e_{z_w}$ are error components of x_w, y_w, z_w, respectively. In previous studies [8]–[10], $e_{x_w}, e_{y_w}, e_{z_w}$ were calculated by

$$e_* = \sqrt{\sum_{i=1}^{N}\left(\frac{\partial\Theta_*}{\partial\delta_i}\right)^2 e_{\delta_i}^2} \tag{5}$$

where e_* represents the three error components $(e_{x_w}, e_{y_w}, e_{z_w})$, $\frac{\partial\Theta_*}{\partial\delta_i} \in (\frac{\partial\Theta_{x_w}}{\partial\delta_i}, \frac{\partial\Theta_{y_w}}{\partial\delta_i}, \frac{\partial\Theta_{z_w}}{\partial\delta_i})$ are the corresponding partial derivatives with respect to ith system parameter δ_i [8]. These derivatives, often called sensitivity coefficients, describe how the output $\Theta_{x_w}, \Theta_{y_w}, \Theta_{z_w}$ varies with changes in the values of the system parameters δ. The error component of the ith parameter in δ is denoted as e_{δ_i}. As indicated in (5), previous studies [8]–[10] all regarded the system parameters δ as uncorrelated (independent) parameters and directly combined the error components e_{δ_i} together.

However, in practice, not all the system parameters δ are independent, and the correlations must be taken into account. There are significant correlations between camera orientation β_L, β_R and the accuracy in detecting corresponding points $(x_L, y_L), (x_R, y_R)$. In the detection of corresponding points $(x_L, y_L), (x_R, y_R)$, camera orientation β_L, β_R introduces deviations as $(\triangle_{x_L}, \triangle_{y_L}), (\triangle_{x_R}, \triangle_{y_R})$. Take ellipse center detection in CCT as an example, a smaller camera orientation angle results in a larger viewing angle with respect to the object, as shown in Fig. 3. A larger viewing angle brings a more severe perspective distortion into the images, which causes deviations $(\triangle_{x_L}, \triangle_{y_L}), (\triangle_{x_R}, \triangle_{y_R})$ in detecting corresponding points $(x_L, y_L), (x_R, y_R)$.

To prove this, as shown in Fig. 3, we rendered synthetic images with multiple circles on a 2-D target under different viewing angles by using MATLAB Graphics tool box. A 3-D mesh model of the 2-D calibration target and a pinhole camera model were used to create the synthetic images. The mesh model emulates the dimensions, color, and surface properties of the calibration target. The camera model has intrinsic parameters taken from a real-world camera (Basler acA2440-20 gm + Computar lens with 16 mm focal length). In order to verify the effect of lens distortions, we also introduce lens distortions in the synthetic experiment. The distortion model has parameters taken from a real-world camera including radial distortion coefficients: $k_1 = -0.076, k_2 = 0.068$ and tangential distortion coefficients: $p_1 = -0.0003, p_2 = -0.0005$. The pose of the mesh model and the extrinsic parameters of the camera were changed to generate different images. The standard center detection algorithm [13] was then applied to extract the center positions. The ground truth center positions were calculated by projecting known 3-D centers in the mesh model onto the 2-D image plane. The deviations in the detected corresponding points $((\triangle_{x_L}, \triangle_{y_L}), (\triangle_{x_R}, \triangle_{y_R}))$ were obtained by subtracting the detected center positions with the ground truth positions. The quantitative relationship between camera orientation and the deviations in the detected corresponding points $(\beta_L \leftrightarrow (\triangle_{x_L}, \triangle_{y_L}))$ is shown in Fig. 3. Note that the same relationship exists for the right camera, i.e., $\beta_R \leftrightarrow (\triangle_{x_R}, \triangle_{y_R})$.

As shown in Fig. 3, a smaller camera orientation angle β_L, β_R caused larger detection deviations $(\triangle_{x_L}, \triangle_{y_L}), (\triangle_{x_R}, \triangle_{y_R})$. Similarly in other applications of SV systems, for instance, camera orientation influences the accuracy in detecting corresponding points $(x_L, y_L), (x_R, y_R)$ in phase decoding of FPP and block matching of DIC. Therefore, ignoring correlations between camera orientation β_L, β_R and the accuracy in detecting corresponding points $(x_L, y_L), (x_R, y_R)$ in previous studies [8]–[10] led to the divergence of optimal camera orientation used in practice and predicted by theory.

Considering the correlation between camera orientation β_L, β_R and the accuracy in detecting corresponding points $(x_L, y_L), (x_R, y_R)$, this article introduces covariance into the error propagation model. Due to the correlation among system parameters δ, the new expression of errors $\hat{e}_* \in (\hat{e}_{x_w}, \hat{e}_{y_w}, \hat{e}_{z_w})$ are

$$\hat{e}_* = \sqrt{\sum_{i=1}^{N} \left(\frac{\partial \Theta_*}{\partial \delta_i}\right)^2 e_{\delta_i}^2 + 2\sum_{i=1}^{N-1}\sum_{j=i+1}^{N} \frac{\partial \Theta_*}{\partial \delta_i}\frac{\partial \Theta_*}{\partial \delta_j} e_{(\delta_i,\delta_j)}^2} \tag{6}$$

where $e_{(\delta_i,\delta_j)}$ is the estimated covariance associated with the ith parameter δ_i and jth parameter δ_j in system parameters δ. According to [5], $e_{(\delta_i,\delta_j)}$ is

$$e_{(\delta_i,\delta_j)} = \sqrt{r_{(\delta_i,\delta_j)} e_{\delta_i} e_{\delta_j}} \tag{7}$$

In the abovementioned equation, $r_{(\delta_i,\delta_j)}$ is the correlation coefficient, which is a measure of the relative mutual dependence of two variables [14]. In this article, $r_{(\delta_i,\delta_j)}$ is a pure number characterizing the degree of correlation between δ_i and δ_j. It satisfies $r_{(\delta_i,\delta_j)} = r_{(\delta_j,\delta_i)}$ and $-1 \le r_{(\delta_i,\delta_j)} \le 1$. If δ_i and δ_j are uncorrelated, $r_{(\delta_i,\delta_j)} = 0$. If correlated, a change $\triangle_{\delta_i}$ in δ_i produces a change $\triangle_{\delta_j}$ in δ_j, and the correlation coefficient $r_{(\delta_i,\delta_j)}$ can be estimated by [14]

$$r_{(\delta_i,\delta_j)} \approx \frac{e_{\delta_i}\ \triangle_{\delta_j}}{e_{\delta_j}\ \triangle_{\delta_i}}. \tag{8}$$

In this article, the system parameters δ include $(x_L, y_L, x_R, y_R, \beta_L, \beta_R, B, f_L, f_R)$. As discussed previously, the correlations between camera orientation $\beta_L(\delta_5), \beta_R(\delta_6)$ and the accuracy in detecting corresponding points $(x_L(\delta_1), y_L(\delta_2)), (x_R(\delta_3), y_R(\delta_4))$ are considered because camera orientation determines the viewing angle, which further causes deviations $(\triangle_{x_L}, \triangle_{y_L}), (\triangle_{x_R}, \triangle_{y_R})$ in detecting corresponding points, as illustrated in Fig. 3. There is no significant correlation among other system parameters. For example, the focal length $(f_L(\delta_8), f_R(\delta_9))$ is determined in calibration and not influenced by other parameters. Thus, four groups of correlation coefficients including $r_{(\delta_1,\delta_5)}, r_{(\delta_2,\delta_5)}, r_{(\delta_3,\delta_6)}$, and $r_{(\delta_4,\delta_6)}$ are used to represent the considered correlations. Since $\triangle_{\delta_5}$, $\triangle_{\delta_6}$ $(\triangle_{\beta_L}, \triangle_{\beta_R})$ and corresponding change $\triangle_{\delta_1}$ $(\triangle_{x_L})$, $\triangle_{\delta_2}$ $(\triangle_{y_L})$, $\triangle_{\delta_3}$ $(\triangle_{x_R})$, and $\triangle_{\delta_4}$ $(\triangle_{y_R})$ can be determined through the proposed image rendering technique, as shown in Fig. 3, according to the definition of $r_{(\delta_i,\delta_j)}$ in (8), the unknown correlation coefficients are obtained. Based on the abovementioned analysis, (6) is rewritten into

$$\hat{e}_{x_w} = \sqrt{J_{x_w} \Lambda J_{x_w}^T},\ \hat{e}_{y_w} = \sqrt{J_{y_w} \Lambda J_{y_w}^T},\ \hat{e}_{z_w} = \sqrt{J_{z_w} \Lambda J_{z_w}^T} \tag{9}$$

where J_{x_w}, J_{y_w}, and J_{z_w} are the input Jacobian matrices, namely, the matrices of partial derivatives $\frac{\partial \Theta_{x_w}}{\partial \delta_i}, \frac{\partial \Theta_{y_w}}{\partial \delta_i}, \frac{\partial \Theta_{z_w}}{\partial \delta_i}$ [8]. The covariance matrix Λ is

$$\Lambda = \begin{bmatrix} e_{\delta_1}^2 & 0 & 0 & 0 & e_{(\delta_1,\delta_5)}^2 & 0 & 0 & 0 & 0 \\ 0 & e_{\delta_2}^2 & 0 & 0 & e_{(\delta_2,\delta_5)}^2 & 0 & 0 & 0 & 0 \\ 0 & 0 & e_{\delta_3}^2 & 0 & 0 & e_{(\delta_3,\delta_6)}^2 & 0 & 0 & 0 \\ 0 & 0 & 0 & e_{\delta_4}^2 & 0 & e_{(\delta_4,\delta_6)}^2 & 0 & 0 & 0 \\ e_{(\delta_5,\delta_1)}^2 & e_{(\delta_5,\delta_2)}^2 & 0 & 0 & e_{\delta_5}^2 & 0 & 0 & 0 & 0 \\ 0 & 0 & e_{(\delta_6,\delta_3)}^2 & e_{(\delta_6,\delta_4)}^2 & 0 & e_{\delta_6}^2 & 0 & 0 & 0 \\ 0 & 0 & 0 & 0 & 0 & 0 & e_{\delta_7}^2 & 0 & 0 \\ 0 & 0 & 0 & 0 & 0 & 0 & 0 & e_{\delta_8}^2 & 0 \\ 0 & 0 & 0 & 0 & 0 & 0 & 0 & 0 & e_{\delta_9}^2 \end{bmatrix}. \tag{10}$$

Note that previous studies all regarded the system parameters δ as uncorrelated parameters and directly combined error components with (5). In this case, the covariance matrix Λ degenerates into a diagonal matrix, which is a special case of our proposed error propagation model.

III. Experimental Results

To verify the effectiveness of the proposed error propagation model, three representative applications of SV systems were investigated, including CCT, FPP, and stereo DIC. A standard SV system consisting of two cameras (Basler acA2440-20 gm, resolution: 2448 × 2048 pixels) with a baseline distance B of 400 mm and two Computar lens with 16 mm focal length was used in experiments. To project fringe and speckle images for FPP and DIC, a Texas Instruments LighterCrafter 4500 projector was installed between the two cameras. As recommended in the previous studies error [8]–[12], symmetrical orientation of the two cameras was adopted, and the camera orientation angles (β_L, β_R) were set to the same value.

CCT is a typical 3-D sparse point reconstruction technique widely used for target tracking and online positioning [1]. The algorithm detects the 2-D center of fiducial markers attached to the target object. The stereo view constraint is used to match the corresponding points for 3-D reconstruction. To evaluate the performance of the proposed error propagation model in CCT, a standard certified 2-D calibration target shown in Fig. 4(a) was used. The distance between two adjacent circles in Fig. 4(a) is known to be 20 ± 0.001 mm. The mean measurement error of the distance between two adjacent circles was used as the metric for evaluation, i.e., $\epsilon_c = \sum_{i=1:N} |d_c^i - 20.0|/N$ in which d_c^i is distance between the ith reconstructed circle center and its immediately adjacent circle center, and N is the number of total points. In the experiment, the proposed error propagation model considering correlated system parameters δ (with and without lens distortions) was compared with the traditional error propagation model reported in previous studies [8]–[10]. In the experiment, we manually increased the camera orientation angle from 40° to 80° with a 10° interval. For each measurement, ten stereo images were captured from different poses and 3-D coordinates of circle centers on the calibration target were reconstructed, and the mean measurement errors ϵ_c were quantified. Fig. 4(d) shows that while the traditional error propagation model suggests the optimal range to be 30°–50°, the experimental data showed that the SV system had the lowest error ϵ_c when the camera orientation angle was 69°. The experimental result is consistent with that proved by our new error propagation model, i.e., the optimal camera orientation angle lies in 60°–80°. To evaluate the performance under lens distortions, the updated covariance matrix Λ was calculated with (6)–(8) with lens distortions considered (see dash lines in Fig. 3). As shown in Fig. 4(d), the difference between the proposed model with lens distortions considered and experimental data is smaller than that of traditional model without involving lens distortions. Note that there is still a small deviation (approximately 0.005 mm) because there are other

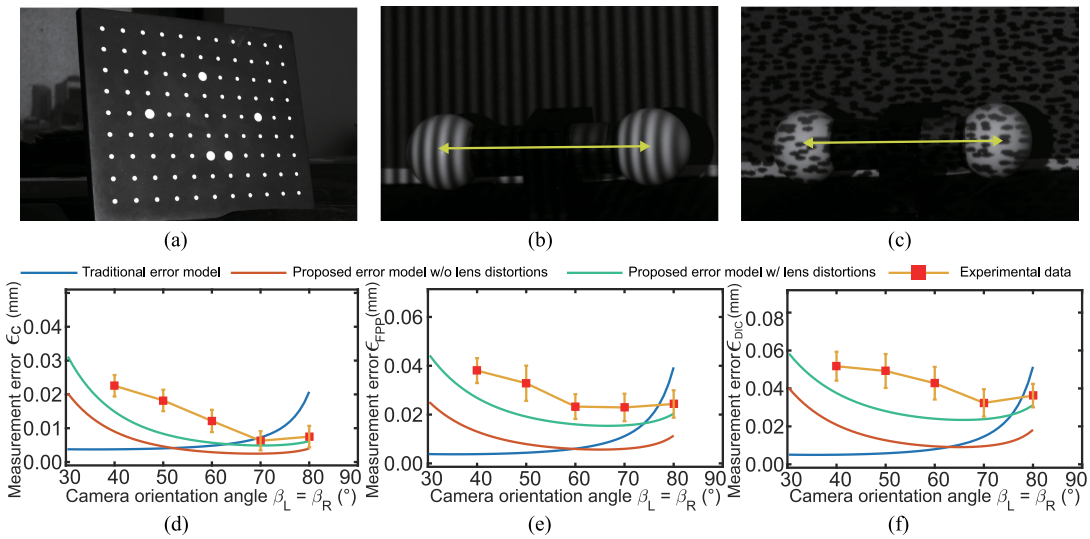

Fig. 4. Representative SV applications for verifying the effectiveness of the proposed error propagation model including (a) CCT for measuring center distance of circles on a calibration target, (b) FPP, and (c) stereo DIC for measuring the center-to-center distance of a CMM verified ball-bar. Correspondingly, experimental data and results from the traditional error propagation model and the proposed error propagation model (w/ and w/o lens distortions) are shown in (d)–(f).

factors, such as noises of the image sensor and camera self-heating, which are difficult to be included in our proposed error propagation model.

To further evaluate the performance of our proposed error propagation model, measurements were made on a certified standard ball-bar using the FPP and DIC techniques. FPP and DIC are two representative techniques of SV systems for dense 3-D reconstruction. DIC is a typical single-shot 3-D reconstruction method [3], in which, a single random speckle image is projected onto the target object for a richer texture. Then DIC finds the maximum of the correlation array between pixel intensity array blocks on stereo images and outputs the corresponding points for 3-D reconstruction. For FPP, it is a typical multiple-shot method [2], which involves projecting a series of coded images (instead of a single random speckle image in DIC) to the target object. Decoding the information from the stereo images results in accurate corresponding points used for 3-D reconstruction. In the experiment, the ball-bar has a known center-to-center distance of $d_b = 100.2073$ mm as verified by a coordinate measuring machine (CMM). The ball-bar was scanned by FPP and DIC. The metric of measurement error were defined as $\epsilon_{\text{FPP}} = |d_{\text{FPP}} - d_b|$ for FPP and $\epsilon_{\text{DIC}} = |d_{\text{DIC}} - d_b|$ for DIC, where ϵ_{FPP} and ϵ_{DIC} are the measured distance. In the experiments, the proposed error propagation model was compared with the traditional error propagation model [8]–[10]. The camera orientation angle was increased from 40° to 80° and at each angle, ten measures were taken to calculate the mean measurement errors ϵ_{FPP} and ϵ_{DIC}. The FPP and DIC experimental results are summarized in Fig. 4(e) and (f), respectively. The results showed that the traditional error propagation model predicted similar accuracies for FPP and DIC, and suggested the optimal camera orientation angle to be 35°–55°. In contrast, our proposed error propagation model suggested 60°–75° as the range for low measurement errors, and the trend of its predicted error was consistent with the experimental results. The results in Fig. 4(e) and (f) indicates that DIC's measurement error is larger than that of FPP. Because DIC relies on surrounding pixels for block matching, the reconstruction accuracy is sacrificed at the discontinuous surfaces or edges. In contrast, FPP uniquely encodes every pixel in the image and maintains the overall accuracy. Similar to the CCT results, the differences between our proposed model with lens distortions considered and experimental data are smaller than those of the previous traditional model without lens distortions considered. Additionally, the experimentally measured errors were slightly larger than the theoretical values from the proposed model because of factors such as noises of image sensor and camera self-heating.

IV. Conclusion

This article proposed a new error propagation model of SV systems. Unlike previous models that treated system parameters δ as uncorrelated, our proposed model introduces covariance to model the correlation between camera orientation β_L, β_R and the accuracy of detecting corresponding points $(x_L, y_L), (x_R, y_R)$. The proposed model proves that the optimal camera orientation angle lies in 60°–80°, which was verified experimentally in this article. This theoretically suggested that the result is consistent with the camera orientation angle typically used in practical SV systems and commercial products.

Acknowledgment

The authors would like to thank the technical support by Mr. C. Zeng and Dr. Y. Lin from Kirchhoff Automobile North America Inc.

References

[1] Z. Chen, D. Zhou, H. Liao, and X. Zhang, "Precision alignment of optical fibers based on telecentric stereo microvision," *IEEE/ASME Trans. Mechatronics*, vol. 21, no. 4, pp. 1924–1934, Aug. 2016.

[2] X. Liu, W. Chen, H. Madhusudanan, J. Ge, C. Ru, and Y. Sun, "Optical measurement of highly reflective surfaces from a single exposure," *IEEE Trans. Ind. Informat.*, early access, Apr. 30, 2020, doi: 10.1109/TII.2020.2991458.

[3] Y. Huang, K.-M. Lee, J. Ji, and W. Li, "Digital image correlation based on primary shear band model for reconstructing displacement, strain and stress fields in orthogonal cutting," *IEEE/ASME Trans. Mechatronics*, vol. 25, no. 4, pp. 2088–2099, Aug. 2020.

[4] G. Di Leo, C. Liguori, and A. Paolillo, "Covariance propagation for the uncertainty estimation in stereo vision," *IEEE Trans. Instrum. Meas.*, vol. 60, no. 5, pp. 1664–1673, May 2011.
[5] R. M. Haralick, "Propagating covariance in computer vision," in *Performance Characterization in Computer Vision*. New York, NY, USA: Springer, 2000, pp. 95–114.
[6] B. Lu, H. K. Chu, K. Huang, and J. Lai, "Surgical suture thread detection and 3D reconstruction using a model-free approach in a calibrated stereo-visual system," *IEEE/ASME Trans. Mechatronics*, vol. 25, no. 2, pp. 792–803, Apr. 2020.
[7] Z. Wang *et al.*, "Digital image correlation in experimental mechanics and image registration in computer vision: similarities, differences and complements," *Opt. Lasers Eng.*, vol. 65, pp. 18–27, 2015.
[8] L. Yang, B. Wang, R. Zhang, H. Zhou, and R. Wang, "Analysis on location accuracy for the binocular stereo vision system," *IEEE Photon. J.*, vol. 10, no. 1, Feb. 2018, Art. no. 7800316.
[9] F. Fooladgar, S. Samavi, S. M. R. Soroushmehr, and S. Shirani, "Geometrical analysis of localization error in stereo vision systems," *IEEE Sensors J.*, vol. 13, no. 11, pp. 4236–4246, Nov. 2013.
[10] W. Sankowski *et al.*, "Estimation of measurement uncertainty in stereo vision system," *Image Vis. Comput.*, vol. 61, pp. 70–81, 2017.
[11] R. Anchini, G. di Leo, C. Liguori, and A. Paolillo, "Metrological characterization of a vision-based measurement system for the online inspection of automotive rubber profile," *IEEE Trans. Instrum. Meas.*, vol. 58, no. 1, pp. 4–13, Jan. 2009.
[12] J. Elizabeth M. C. and M. A. Iadicola, "A good practices guide for digital image correlation," *Int. Digit. Image Correlation Soc.*, p. 7, 2018.
[13] C. Lu, S. Xia, M. Shao, and Y. Fu, "Arc-support line segments revisited: An efficient high-quality ellipse detection," *IEEE Trans. Image Process.*, vol. 29, pp. 768–781, Aug. 2019.
[14] W. Bich *et al.*, "Towards a new guman update," *Metrologia*, vol. 53, no. 5, pp. S149–S159, 2016.